

See discussions, stats, and author profiles for this publication at: <https://www.researchgate.net/publication/49736405>

Factors Controlling Stripping Voltammetry of Lead at Polycrystalline Boron Doped Diamond Electrodes: New Insights from High-Resolution Microscopy

ARTICLE *in* ANALYTICAL CHEMISTRY · FEBRUARY 2011

Impact Factor: 5.64 · DOI: 10.1021/ac101626s · Source: PubMed

CITATIONS

21

READS

35

4 AUTHORS, INCLUDING:



Laura A Hutton

Element Six

11 PUBLICATIONS 238 CITATIONS

[SEE PROFILE](#)



Mark Edward Newton

The University of Warwick

105 PUBLICATIONS 1,783 CITATIONS

[SEE PROFILE](#)



Julie V Macpherson

The University of Warwick

175 PUBLICATIONS 5,618 CITATIONS

[SEE PROFILE](#)

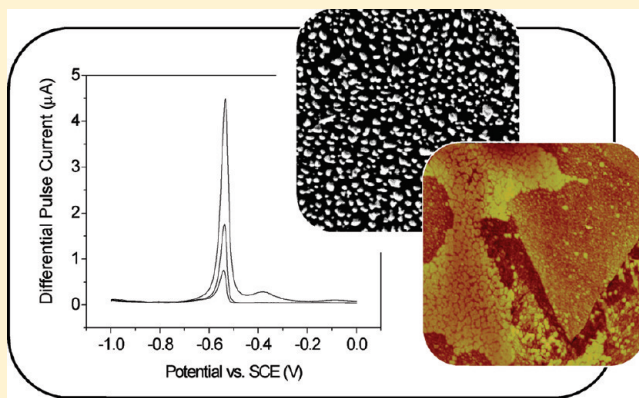
Factors Controlling Stripping Voltammetry of Lead at Polycrystalline Boron Doped Diamond Electrodes: New Insights from High-Resolution Microscopy

Laura A. Hutton,[†] Mark E. Newton,[‡] Patrick R. Unwin,^{†,*} and Julie V. Macpherson^{†,*}

[†]Departments of Chemistry and [‡]Physics, University of Warwick, Coventry CV4 7AL, United Kingdom

 Supporting Information

ABSTRACT: We report wide-ranging studies to elucidate the factors and issues controlling stripping voltammetry of metal ions on solid electrodes using the well-known Pb/Pb²⁺ couple on polycrystalline boron doped diamond (pBDD) as an exemplar system. Notably, high-resolution microscopy techniques have revealed new insights into the features observed in differential pulse anodic stripping voltammetry (DPV–ASV) which provide a deeper understanding of how best to utilize this technique. DPV–ASV was employed in an impinging wall-jet configuration to detect Pb²⁺ in the nanomolar to micromolar concentration range at a pBDD macrodisk electrode. The deposition process was driven to produce a grain-independent homogeneous distribution of Pb nanoparticles (NPs) on the electrode surface; this resulted in the observation of narrow stripping peaks. Lower calibration gradients of current or charge versus concentration were found for the low concentrations, correlating with a lower than expected (from consideration of the simple convective-diffusive nature of the deposition process) amount of Pb deposited on the surface. This was attributed to the complex nature of nucleation and growth at solid surfaces in this concentration regime, complicating mass transport. Furthermore, a clear shift negative in the stripping peak potential with decreasing concentration was seen correlating with a change in the size of the deposited NP, suggesting an NP size-dependent redox potential for the Pb/Pb²⁺ couple. At high concentrations a nonlinear response was observed, with less Pb detected than expected, in addition to the observation of a second stripping peak. Atomic force microscopy (AFM) and field emission scanning electron microscopy revealed the second peak to be due to a change in deposition morphology from isolated NPs to grain-independent heterogeneous structures comprising both thin films and NPs; the second peak is associated with stripping from the thin-film structures. AFM also revealed a substantial amount of Pb remaining on the surface after stripping at high concentration, explaining the nonlinear relationship between stripping peak current (or charge) and concentration. Finally, the use of an *in situ* cleaning procedure between each measurement was advocated to ensure a clean Pb-free surface (verified by AFM and X-ray photoelectron spectroscopy analysis) between each run. The studies herein highlight important and complex physicochemical processes involved in the electroanalysis of heavy metals at solid electrodes, such as pBDD, that need to be accounted for when using stripping voltammetry methods.



Anodic stripping voltammetry (ASV) is well-established for the detection of heavy metals.¹ The analyte of interest is reduced at the electrode surface in a preconcentration step, followed by anodic sweeping of the electrode potential to oxidatively strip reduced analyte from the surface in a quantifiable way.¹ Until recently, Hg films² and drops³ have been the electrodes of choice for trace-level metal detection, offering sub parts per billion detection limits.⁴ Hg is particularly attractive as an electrode material, as it has a wide cathodic potential window, enabling metal deposition via reduction without hydrogen evolution at the electrode. Furthermore, because it is liquid at room temperature, Hg—metal amalgams result, following reduction of the metal of interest. Thus, during stripping, symmetrical voltammetric peaks are typically obtained,

characterized with defined widths at half-height, due to the “homogeneous” nature of the Hg electrode. However, the toxicity of Hg is now of great concern, and alternative nontoxic electrode materials for heavy-metal detection are highly sought.^{5,6}

One of the most important considerations for a Hg replacement electrode is the need for a wide cathodic potential window. Polycrystalline boron doped diamond (pBDD) is currently attracting much attention due to its very wide potential window in aqueous solution, low background currents, and resistance to fouling.^{7–9} pBDD is also resistant to corrosion under both acidic

Received: June 20, 2010

Accepted: December 10, 2010

Published: January 7, 2011

and alkaline conditions, as well as at extreme potentials,¹⁰ and is stable at high temperatures and pressures. pBDD has been used with different ASV techniques, including linear sweep voltammetry (LSV),¹¹ differential pulse voltammetry (DPV),^{12,13} and square-wave voltammetry,¹⁴ to detect a wide range of heavy metals. These include, for example, Zn, Cd, Pb, and Cu, down to parts per billion levels in electrolyte solutions, lake and tap water, river sediment, and wastewater sludge.^{14–16}

In contrast to those obtained on Hg electrodes, the stripping peaks obtained on pBDD electrodes are often broad and largely asymmetric.^{12,13,16} This has been attributed to the use of (i) a heterogeneously active solid electrode where the different crystallographically orientated grains are characterized by different electrical conductivity and surface structure¹⁷ and (ii) a heterogeneous size distribution of electrodeposited structures.^{15,18} In general, dependent on the solution conditions, applied potential, time, and structure of the pBDD surface (e.g., grain size, surface roughness, and surface termination),^{17,19–21} a wide variation in electrodeposited metal particle size and surface morphology has been reported using electron microscopy and atomic force microscopy (AFM). However, to date, there have been no high-resolution microscopy studies of the effect of anodic stripping on the electrodeposited metal structures that form during stripping voltammetry. Speculation on stripping-induced changes in the metal surface morphology is often inferred from indirect analysis of the current–voltage (or time) response.

Double stripping peaks have been observed for anodic metal dissolution at relatively high metal ion concentrations (e.g., >100 ppb for the case of Pb¹⁵), attributed loosely to the “nature” of the metal deposit on the surface (no microscopic evidence was presented).¹⁵ The majority of previous studies also report an excess charge associated with deposition compared to stripping.^{13,22–24} This has been attributed to several factors: (i) incomplete metal stripping, (ii) detachment of metal particles from the electrode surface,^{25,26} and (iii) hydrogen evolution during deposition,¹² catalyzed by the deposited metallic nanostructures. Again, however, a lack of complementary microscopic investigation means that these suggestions remain conjectures.

Given the current level of understanding of ASV on pBDD, the goal of this study is to develop new insights into the deposition and stripping process, particularly through the use of AFM. Herein, we investigate the electrodeposition and stripping behavior of Pb²⁺/Pb at pBDD electrodes for Pb²⁺ concentrations in the nanomolar to micromolar range. This system was selected for detailed investigation as it is among the most studied, but as highlighted, there are many questions regarding DPV–ASV analysis that are yet to be answered. The aim is to correlate the observed current response with metal nucleation/growth and dissolution mechanisms. To increase mass transport during the deposition step^{27–31} (and reduce deposition times), we use an impinging jet setup,^{32,33} which has well-characterized hydrodynamics,³⁴ to deliver solution to the pBDD electrode.

■ EXPERIMENTAL SECTION

Solutions. All solutions were prepared from Milli-Q water (Millipore Corp.), resistivity 18.2 MΩ cm at 25 °C. All reagents were used as received and included potassium nitrate (Aldrich, 99%) and lead nitrate (Aldrich 99.99%). The concentration of Pb²⁺ in the lead nitrate solutions was verified using an Agilent Technologies 7500cs inductively coupled plasma mass spectrometer. The pH of the resulting solutions was ~6.3.

pBDD Material and Properties. The pBDD samples were prepared by Element Six Ltd. (E6 Ltd., Ascot, U.K.) using a commercial microwave plasma chemical vapor deposition process, developed in-house. The average boron doping level of this material was ca. 5×10^{20} atoms cm⁻³, as determined by secondary ion mass spectroscopy. The pBDD samples were lapped by E6 Ltd. to give a 500 μm thick sample with typical grain sizes, as measured by field emission scanning electron microscopy (FE-SEM), of ca. 2–20 μm. Lapping involves a polishing process in which the pBDD is rotated and translated while in contact with a spinning polishing wheel. Since diamond has highly anisotropic hardness/wear rates and the pBDD is made up from differently orientated grains, this approach is necessary to achieve low-roughness surfaces. Typical AFM and FE-SEM images of the pBDD used in this study, recorded in the same area, are shown in Figure 1.

Electron microscopy (EM) studies of pBDD have shown that secondary electron emission yields from BDD reach a maximum at boron concentrations of $10^{19}–10^{20}$ cm⁻³.³⁵ In previous work we showed unambiguously, for a very similar pBDD material, that the dark regions in the FE-SEM images correlated with the more highly boron doped regions, as confirmed by cathodoluminescence and conducting AFM maps recorded in the same area.¹⁷ The change in dopant levels across the surface is likely to be associated with grain-dependent boron uptake, as it is well-known that boron is more readily incorporated, by a factor of approximately 10, into (111) growth sectors than (100) sectors.³⁶

Interestingly, in Figure 1 it can also be seen that the darker, more highly doped regions in the FE-SEM image also correlate with the lower lying regions in the AFM image. For example, the cross section below Figure 1a shows a height difference, ca. 6 nm, associated with moving across one grain to the next, which the FE-SEM image indicates is a transition from a less doped grain to one which is more doped. The change in height between differently doped regions could be a result of differently orientated crystal grains, or grains with different boron dopant levels polishing at slightly different rates;³⁷ this is currently under further investigation. On the surface of a grain, AFM reveals a surface roughness of ca. 1–2 nm. Thus, from FE-SEM images and AFM height images, it is possible to qualitatively infer how boron uptake across the surface of pBDD varies. As discussed herein, this is important when elucidating whether differently doped grains show particular characteristics in the metal deposition and stripping process.

pBDD Disk Electrode Fabrication. Stripping analysis of Pb²⁺ was performed using 1 mm diameter pBDD disk electrodes. The as-supplied pBDD was laser micromachined (Oxford Lasers E Series) and sealed in glass in-house.²⁰ For AFM analysis, it was necessary to prepare the electrode in a slightly different way to allow subsequent imaging of the surface. The Au/Ti back-contacted pBDD columns²⁰ were annealed on a flat quartz disk which had also been sputtered with Ti/Au. A conducting wire was then adhered to the Au contact on the quartz using silver Electrodag (Agar Scientific, U.K.). Finally, epoxy resin (Aralite, Bostik Findley, U.K.) was used to seal around the edges of the pBDD column and the quartz so that only the pBDD disk was left exposed to electrolyte solution.

Electrochemical Measurements. All electrochemical measurements using the pBDD electrodes were made in three-electrode mode using a potentiostat (CHI730A, CH Instruments Inc., Texas) connected to a laptop computer. A saturated calomel electrode (SCE) was used as a reference electrode, with a Pt gauze serving as a counter electrode. The setup for the impinging wall-jet measurements is shown schematically in Figure 2.

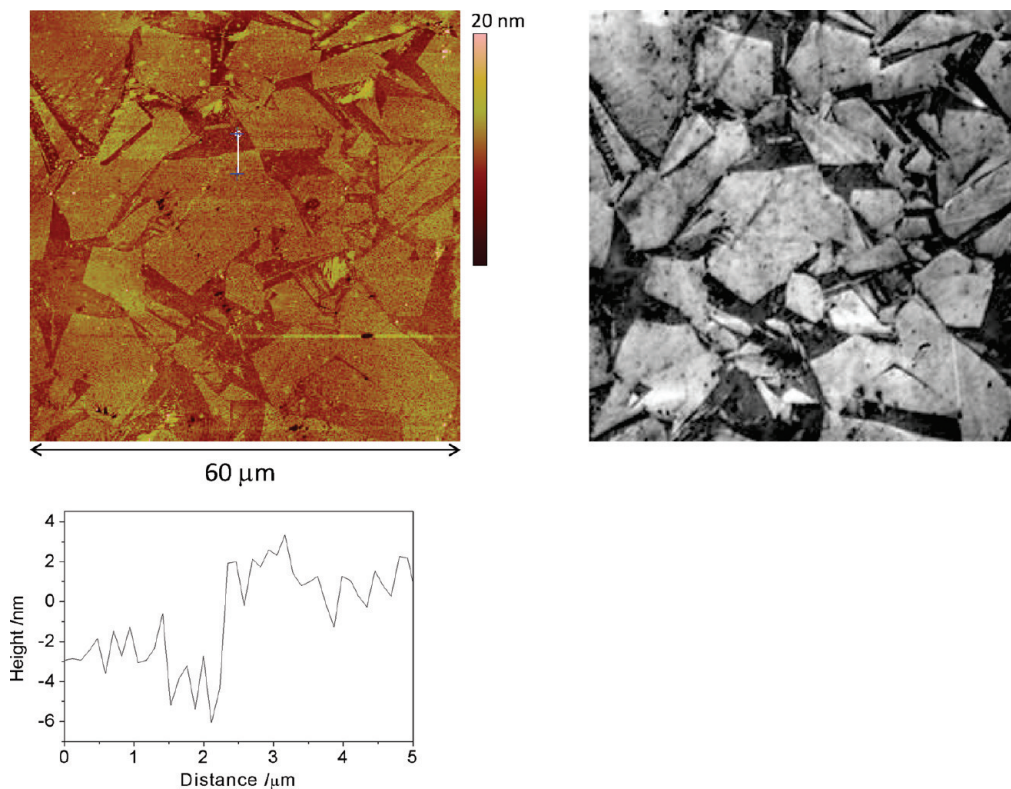


Figure 1. Typical $60\text{ }\mu\text{m} \times 60\text{ }\mu\text{m}$ (a, left) tapping mode AFM height image and (b, right) FE-SEM image of the surface of the lapped pBDD used in these studies. In (a), as indicated by the white line, a height cross-section is shown across two neighboring grains, which as shown by the contrast difference in FE-SEM contain different boron dopant levels.

Typically, during deposition, solution was flowed onto the electrode from a coaxial nozzle^{32,34} of $50\text{ }\mu\text{m}$ inner diameter, placed $500\text{ }\mu\text{m}$ from the pBDD surface, at a flow rate of 0.1 mL s^{-1} . For this sized nozzle, a nozzle–electrode separation of $500\text{ }\mu\text{m}$ was found to give the maximum peak response during stripping. Mass transport in this arrangement was characterized using the steady-state limiting current response for the diffusion-controlled one-electron reduction of $0.1\text{ mM Ru(NH}_3)_6^{3+}$ in 0.1 M KNO_3 as a function of the volume flow rate (over the range $0.025\text{--}0.5\text{ mL min}^{-1}$). As shown in the Supporting Information, section 1, the response correlated extremely well with that expected for a wall-jet electrode arrangement.³⁸

During deposition, the pBDD electrode was held at -1.5 V to drive the electroreduction process. DPV stripping was employed under quiescent conditions in 2 mV steps, with a pulse width and amplitude of 50 ms and 50 mV , respectively.

Surface Characterization. All AFM images of Pb deposition/stripping were recorded either ex situ or in situ at a distance of $\sim 250\text{ }\mu\text{m}$ away from the center of the pBDD electrode in tapping mode using a Veeco Enviroscope AFM instrument with a Nanoscope IV controller. For the impinging jet arrangement, this distance represented the average diffusion length (flux) of the jet profile impinging on the electrode (as discussed further in the Supporting Information, section 2). For the in situ electrochemical AFM measurements, deposition and stripping were carried out in the same location in stationary solution. During stripping, the tip was retracted from the surface and then re-engaged to image the resulting surface structure.

FE-SEM images were recorded using an in-lens detector at 5 kV (Zeiss Supra55VP) to visualize the pBDD grain structure and

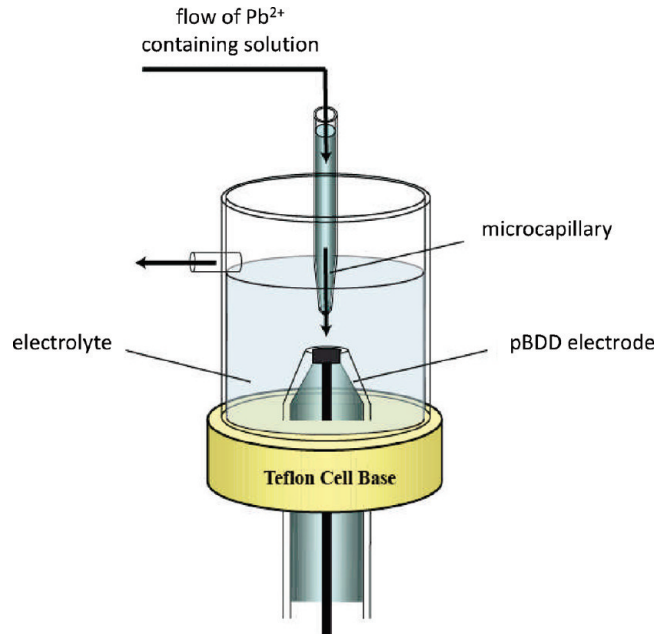


Figure 2. Schematic of the impinging jet arrangement for hydrodynamic delivery of solution to a macrodisk pBDD electrode.

a secondary electron detector at 2 kV to image the Pb deposits. X-ray photoelectron spectroscopy (XPS) chemical analysis was performed using a monochromated $\text{Al K}\alpha$ X-ray source and an EA 124 analyzer (Omicron, Germany).

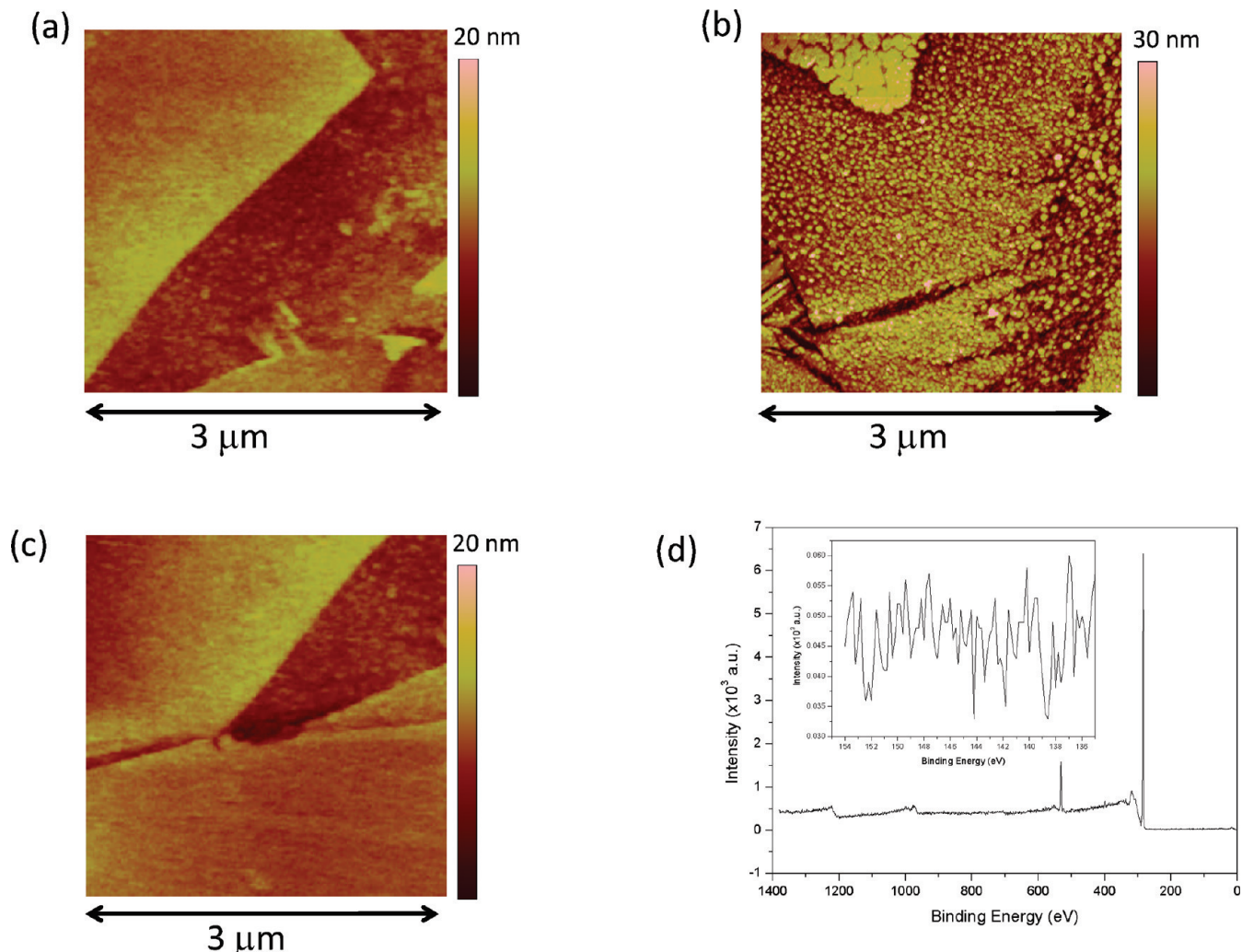


Figure 3. Typical ex situ EC-AFM $3\text{ }\mu\text{m} \times 3\text{ }\mu\text{m}$ height images of a pBDD surface (a) prior to electrodeposition, (b) after deposition of $1\text{ }\mu\text{M}\text{ Pb}^{2+}$ (deposition parameters were 400 s deposition at -1.5 V (vs SCE) with a volume flow rate of 0.1 mL s^{-1}), and (c) after in situ cleaning of the surface ($+1.2\text{ V}$ for 600 s). (d) XPS survey spectra of the electrode after in situ cleaning of the surface, with the inset showing the Pb 4f signature region.

RESULTS AND DISCUSSION

In Situ Cleaning of the pBDD Electrode. To carry out multiple (repetitive) stripping voltammetry measurements on the same electrode, without needing to mechanically clean between each measurement, an in situ electrochemical cleaning process was developed. The aim was to provide a clean and reproducible surface for the start of each measurement, ensuring that no Pb remained on the surface from a previous voltammetric analysis.¹¹ We selected a convenient cleaning time of 10 min and then determined the potential required to achieve a clean, Pb-free surface.

Figure 3 shows typical $3\text{ }\mu\text{m} \times 3\text{ }\mu\text{m}$ ex situ AFM height images of the pBDD electrode surface recorded *in air* for the following situations: (a) prior to electrodeposition, (b) after deposition of $1\text{ }\mu\text{M}\text{ Pb}^{2+}$ (-1.5 V for 400 s) using the impinging jet arrangement, and (c) after application of a potential of $+1.2\text{ V}$ to the electrode surface for 600 s to remove electrodeposited Pb by oxidation. At this potential ($+1.2\text{ V}$), protons are also generated and bubbles of oxygen evolved (to further aid Pb dissolution). A high concentration of Pb was deliberately employed for the deposition step to demonstrate the effectiveness of

the in situ electrochemical cleaning process. Figure 3 d shows an XPS spectrum of the pBDD electrode after cleaning using the in situ protocol. The inset shows the binding energy region which is most sensitive to the presence of Pb.

It is evident from Figure 3 b that electrodeposition of Pb results in extensive coverage of the pBDD surface in Pb nanoparticles (NPs), here with an average height of $19 \pm 7\text{ nm}$ (SD) and coverage of $160 \pm 12\text{ NPs }\mu\text{m}^{-2}$. Importantly, comparison of parts a and c of Figure 3 highlights that pBDD is returned to a pristine state after the in situ electrochemical cleaning process, proving that the deposited Pb NPs can be removed effectively. This is further confirmed by the XPS spectrum of the electrode after the in situ cleaning process. The Pb 4f spectral region (inset to Figure 3 d) shows no detectable signal for Pb; only XPS signatures for carbon and oxygen are present at ~ 284 and $\sim 532\text{ eV}$ corresponding to the C 1s and O 1s orbitals, respectively. This is as expected for a clean oxygen-terminated sp^3 carbon surface.³⁹

Finally, the cleaning procedure could be used repeatedly on the pBDD electrode with no deterioration in the performance of the electrode. Furthermore, the DPV signal (in background electrolyte), after cleaning in this way, was essentially analogous to that for a freshly polished electrode.

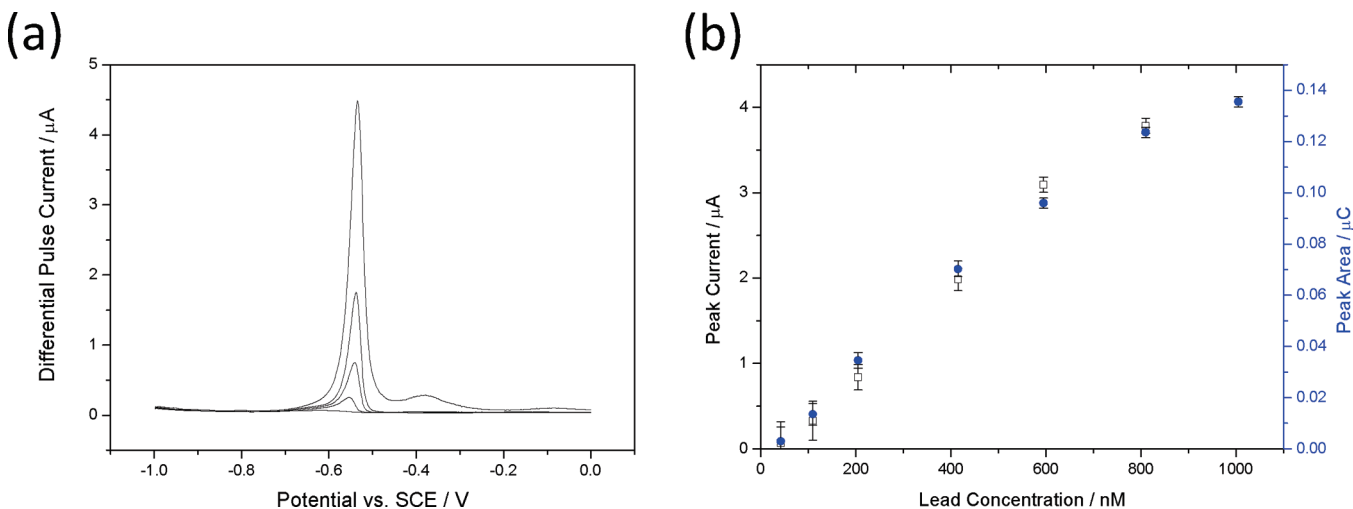


Figure 4. (a) DPV (pulse width, 50 mV; pulse amplitude, 50 mV; step size, 2 mV) in 0.1 M KNO₃ for 42 (lowest curve), 110, 205, 415, and 1005 (highest curve) nM Pb²⁺. Deposition parameters were 400 s at −1.5 V (vs SCE) with a volume flow rate of 0.1 mL s^{−1}. Between each measurement, the pbDD electrode was cleaned in situ. (b) Calibration plot of the peak current (□) and peak area (blue solid circle) versus Pb²⁺ concentration for the Pb²⁺ concentrations shown in (a). All curves have been background corrected.

Impinging Jet-Differential Pulse Stripping Voltammetry. Figure 4 a shows a selection of typical DPV curves for Pb stripping analysis in 0.1 M KNO₃ for [Pb²⁺] in the range from 40 nM to 1 μM. For each concentration, deposition occurred for a period of 400 s at a potential of −1.5 V versus SCE, sufficient to cause the diffusion-limited reduction of Pb²⁺ to Pb at the pbDD electrode. During deposition, solution was flowed onto the electrode using the parameters described in the Experimental Section. Figure 4b shows a corresponding plot of the DPV peak current (black) and area under the peak (blue) versus [Pb²⁺]. The charge data (i.e., area under the DPV peak or peaks) takes into account all areas above the background baseline.

For Pb²⁺ concentrations in the range of 40–800 nM, a single DPV stripping peak was observed, occurring at similar potentials (between −0.53 and −0.55 V) at all but the lowest concentration. At the highest concentration of 1 μM, a second stripping peak appeared at −0.38 V. As the concentration was increased further, the magnitude of this second peak was also found to increase (as shown in the Supporting Information, section 3). The plot in Figure 4b shows a linear relationship between either peak current or peak area and [Pb²⁺], within a defined concentration range of ~100 to ~700 nM. For the two-peak DPV behavior (1 μM Pb²⁺), only the peak area data have been included in Figure 4b. In the linear concentration region, gradients of 4.6 nA nM^{−1} (peak current) and 16.3 nC nM^{−1} (peak area) were obtained.

To detect lower [Pb²⁺] accurately, longer preconcentration times were necessary. Figure 5a shows a selection of typical DPV curves for [Pb²⁺] in the range of 4–100 nM. Deposition occurred with the impinging jet arrangement with the electrode held at −1.5 V versus SCE for 800 s. Within this concentration range, only one stripping peak was observed, which was seen to shift slightly to more negative potentials with decreasing concentration. For example, the peak DPV potentials for 100, 40, and 4 nM Pb were −0.54, −0.58, and −0.62 V, respectively.

Figure 5b summarizes the data as plots of both the peak current (black) and area under the peak (blue) versus [Pb²⁺] for concentrations as low as 4 nM (1 ppb), which are linear, with gradients of 3.4 nA nM^{−1} and 12.4 nC nM^{−1}. Taking into account

the proportionality between the stripping peak charge/current and deposition time,^{1,4} the calibration slopes from Figure 5b (lower concentration range) are smaller than expected on the basis of those obtained from the linear region in Figure 4b (higher concentration range). The reasons for this are considered further below.

Ex Situ Electrochemical AFM. Ex situ AFM was employed to image the pbDD surface after both Pb deposition and stripping to explore further (i) the nonlinearity of the relationship between the charge (or peak current) and concentration at high [Pb²⁺] (Figure 4b and Supporting Information, section 3), (ii) the double stripping peak behavior, observed at high [Pb²⁺] in Figure 4a and the Supporting Information, section 3, (iii) the negative shift in peak potential with decreasing [Pb²⁺] at low concentrations (Figure 5a), and (iv) the lower calibration gradient obtained for lower [Pb²⁺]. Figure 6 shows typical 1 μm × 1 μm AFM height images of the pbDD electrode after (a) deposition of Pb and (b) subsequent DPV stripping. For deposition, the impinging jet arrangement was employed using the same conditions as for Figure 4a for [Pb²⁺] = (i) 1 μM (ii) 100 nM, and (iii) 10 nM.

The effect of [Pb²⁺] on the morphology of electrodeposited Pb can clearly be seen by comparing the images in Figure 6a(i,ii, iii). In Figure 6a(i) for [Pb²⁺] = 1 μM, extensive filmlike islands of Pb are observed on the surface. In contrast, for lower [Pb²⁺], i.e., 100 nM (a(ii)) and 10 nM (a(iii)), Pb NPs with heights of 18 ± 5.2 nm (SD) and 5 ± 1.3 nm (SD) and NP densities of 165 and 142 μm^{−2}, respectively, are homogeneously dispersed across the pbDD surface. The relatively homogeneous distribution of NP sizes is also reflected in the narrow stripping peak widths of the DPV signature.^{15,18,40} We achieve this here for the case of [Pb²⁺] = 10 nM and 100 nM through the use of a high driving force (large overpotential) to ensure a high nucleation rate and thus a high density of small particles.²⁰ Others have advocated the use of pulsed galvanostatic deposition to achieve NPs with a narrow size distribution.¹⁵

It is thus clear that, as [Pb²⁺] decreases, for the deposition potential and time considered, smaller isolated NPs form. This is consistent with work using other metals on highly oriented pyrolytic graphite electrode surfaces.⁴¹ The AFM images in

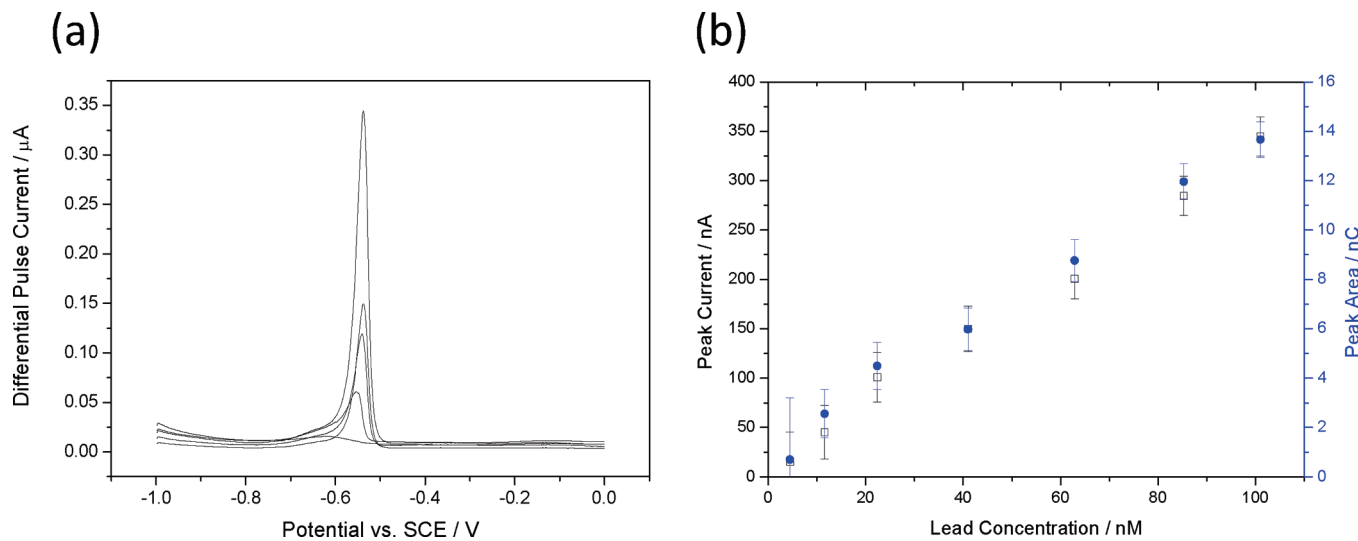


Figure 5. (a) DPV (pulse width, 50 mV; pulse amplitude, 50 mV; step size, 2 mV) in 0.1 M KNO₃ for 4.5 (lowest curve), 11.6, 22.4, 41, and 101 (highest curve) nM Pb²⁺. Deposition parameters were 800 s at −1.5 V (vs SCE) with a volume flow rate of 0.1 mL s^{−1}. Between each measurement, the pBDD electrode was cleaned in situ. (b) Calibration plot of the peak current (□) and peak area (blue solid circle) versus Pb²⁺ concentration for the Pb²⁺ concentrations shown in (a).

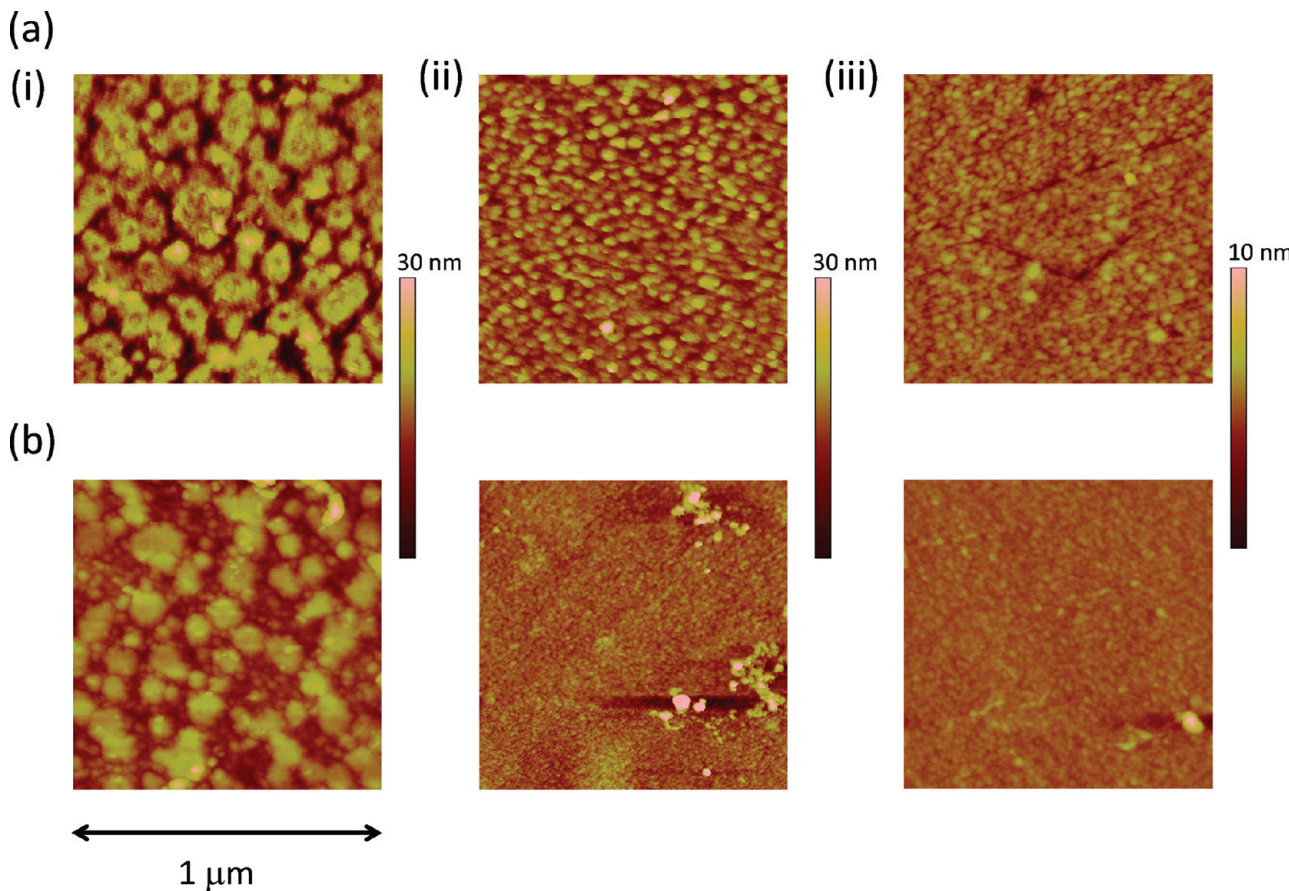


Figure 6. Typical 1 μm × 1 μm ex situ EC-AFM height images of the surface of a pBDD electrode after (a) Pb deposition for 400 s at −1.5 V (vs SCE) with a volume flow rate of 0.1 mL s^{−1} and (b) Pb stripping using DPV at 200 mV s^{−1} (pulse width, 50 mV; pulse amplitude, 50 mV) in 0.1 M KNO₃ at (i) 1 μM Pb²⁺, (ii) 100 nM Pb²⁺, and (iii) 10 nM Pb²⁺.

Figure 6a also provide evidence that the shift in the stripping peak potential with decreasing [Pb²⁺] (Figures 4a and 5a) is most likely related to an NP size-dependent redox potential⁴² for the

Pb/Pb²⁺ couple. Similar shifts were seen for the Cd/Cd²⁺ couple on BDD with decreasing [Cd²⁺],¹⁴ but no explanation was provided as to why this occurred.

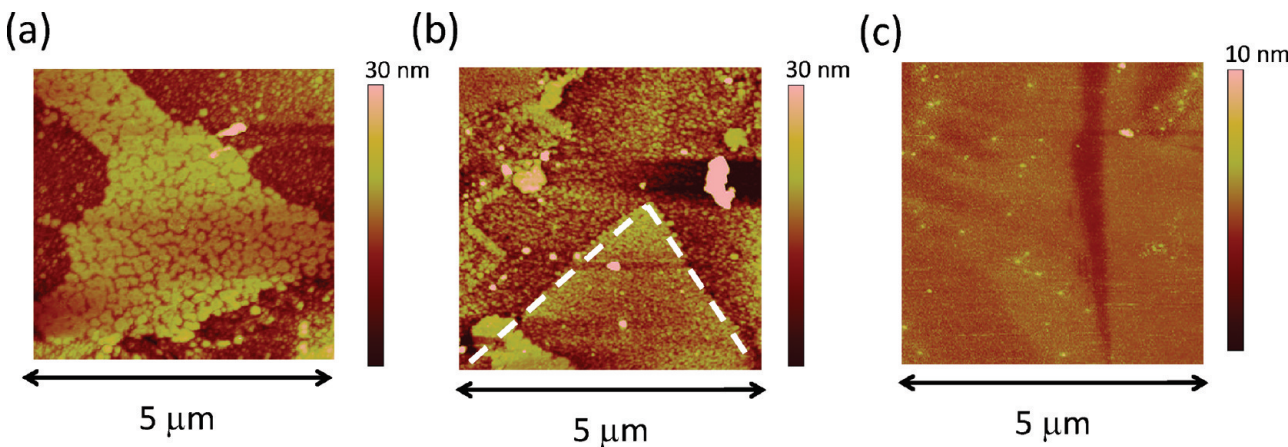


Figure 7. Typical $5\text{ }\mu\text{m} \times 5\text{ }\mu\text{m}$ ex situ EC-AFM images of the surface of a pBDD electrode after electrodeposition of Pb for 400 s at -1.5 V (vs SCE) with a volume flow rate of 0.1 mL s^{-1} for (a) $1\text{ }\mu\text{M Pb}^{2+}$, (b) 100 nM Pb^{2+} , and (c) 10 nM Pb^{2+} . The dashed white line denotes the border of a grain.

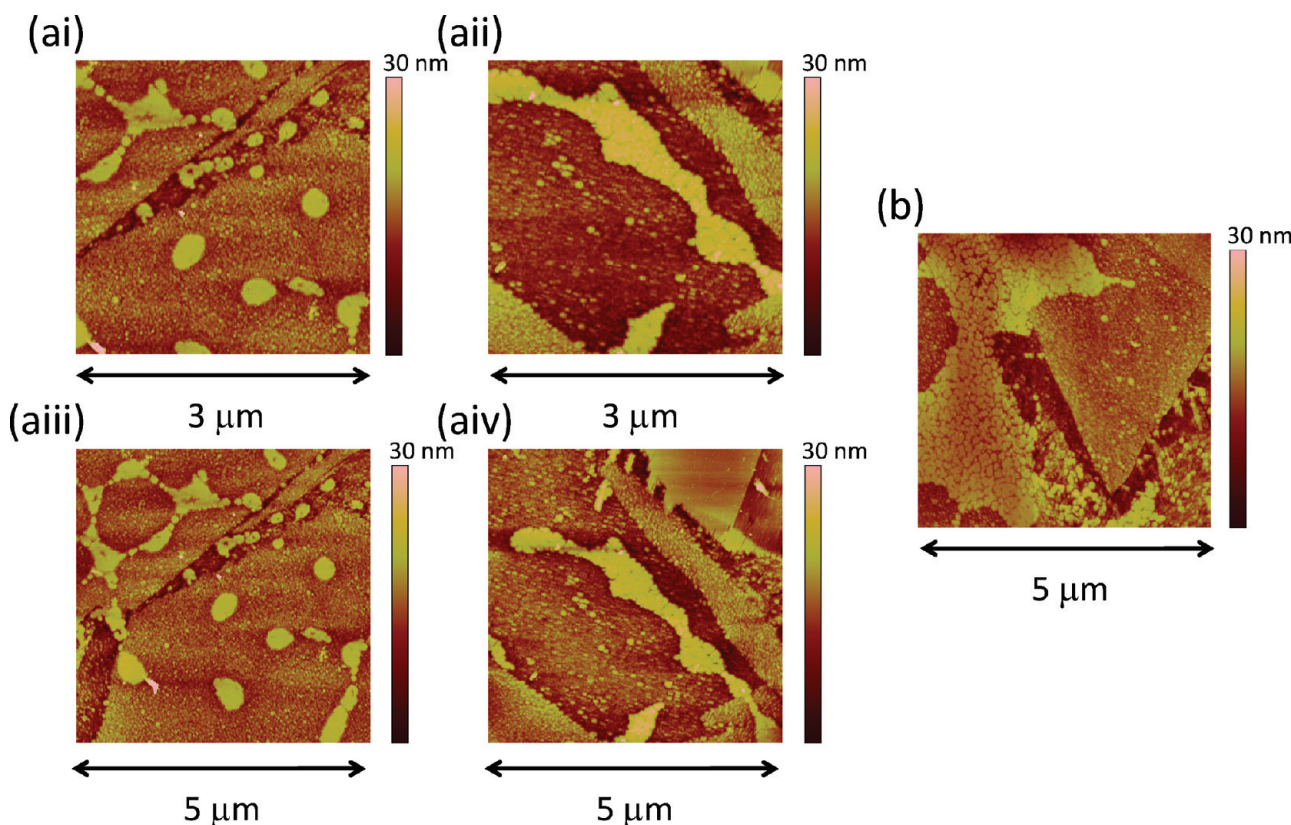


Figure 8. Typical ex situ EC-AFM images of the surface of the pBDD electrode after electrodeposition of $1\text{ }\mu\text{M Pb}^{2+}$ at -1.5 V (vs SCE), with $V_f = 0.1\text{ mL s}^{-1}$, recorded after (a) 300 s and (b) 400 s.

It is informative to calculate the quantity of Pb deposited on the pBDD surface during the deposition step and compare this value to the amount estimated by AFM analysis. This can be done readily for $[\text{Pb}^{2+}] = 100$ and 10 nM , where isolated NPs are evident. The charge associated with Pb deposited on the pBDD electrode was estimated from the average of several AFM images of NP deposition. As it was not possible to unambiguously determine the true geometry of the NPs from the AFM images, the particles were assumed to be both hemispherical (upper charge limit) and spherical (lower charge limit). Note there was

no significant pBDD grain dependence of the Pb NP size and surface coverage (vide infra).

Values of $16.7 \pm 0.8\text{ }\mu\text{C}$ (hemisphere), $4.2 \pm 1.9\text{ }\mu\text{C}$ (sphere) and $0.5 \pm 0.02\text{ }\mu\text{C}$ (hemisphere), $0.09 \pm 0.04\text{ }\mu\text{C}$ (sphere) were estimated from the AFM images for the 100 and 10 nM solutions, respectively. Values of $22.5\text{ }\mu\text{C}$ (100 nM) and $2.3\text{ }\mu\text{C}$ (10 nM) were calculated from consideration of the limiting current at the pBDD (eq S1 in the Supporting Information, section 1) for Pb deposition in a wall-jet configuration,³⁸ assuming diffusion-limited deposition⁴³ and that D for Pb^{2+} is $1.34 \times 10^{-5}\text{ cm}^2\text{ s}^{-1}$.⁴⁴

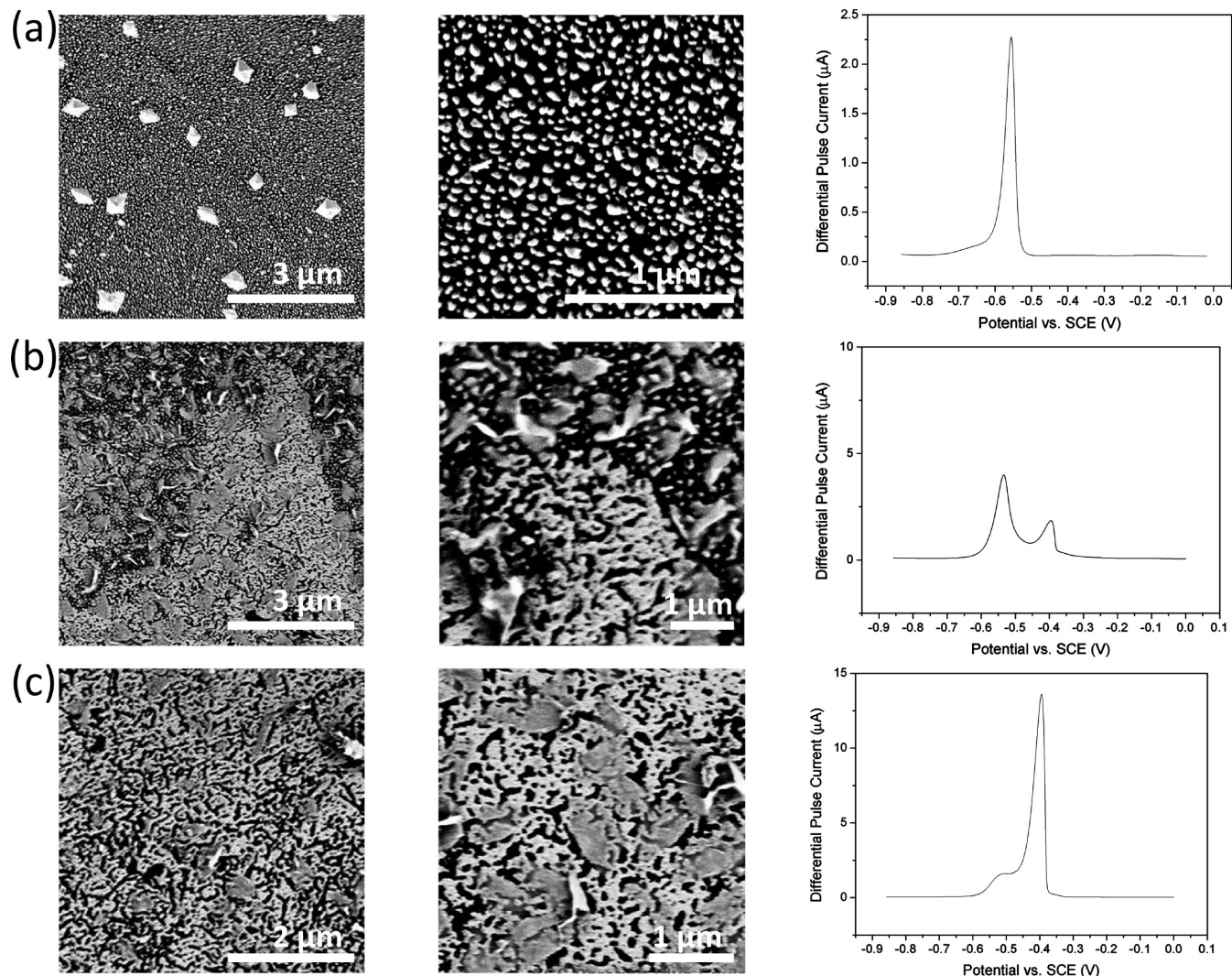


Figure 9. Typical FE-SEM images of the pBDD electrode after Pb deposition for 400 s at -1.5 V (vs SCE), with $V_f = 0.1\text{ mL s}^{-1}$, with the associated DPV response (pulse width, 50 mV; pulse amplitude, 50 mV; step size, 2 mV) in 0.1 M KNO₃ for (a) 0.5 μM Pb²⁺, (b) 10 μM Pb²⁺, and (c) 30 μM Pb²⁺.

The experimental and theoretical charge comparisons are much closer for $[\text{Pb}^{2+}] = 100\text{ nM}$ than for $[\text{Pb}^{2+}] = 10\text{ nM}$. Moreover, the data obtained at 100 nM are more consistent with hemispherical-shaped NPs. One reason for the higher estimate of Pb on the surface, as predicted from the diffusion-limited current, compared to that measured by AFM could be particle instability for smaller NPs on the pBDD surface under the hydrodynamic conditions of the impinging jet. Additionally, or alternatively, at very low concentrations, there is likely to be a more significant induction time for the nucleation of NPs on pBDD which is not taken into account when using eq S1 (Supporting Information) to calculate the charge passed for deposition. Such effects are unimportant for ASV at Hg or Hg film electrodes but are clearly an issue for heterogeneous nucleation and growth on any solid electrode. This issue does not, hitherto, appear to have been adequately considered, and the studies herein highlight the general need for further fundamental studies of metal nucleation and growth from very low concentration solutions.

Typical $1\text{ }\mu\text{m} \times 1\text{ }\mu\text{m}$ AFM height images of the surface after DPV at $[\text{Pb}^{2+}]$ of (i) 1 μM , (ii) 100 nM, and (iii) 10 nM are shown in Figure 6b. After dissolution, the size of the islands in Figure 6b(i) has clearly decreased, with smaller particles now

evident in the background. However, the striking feature is that a substantial amount of Pb remains on the surface which is not detected in the DPV. In contrast, for both panels ii and iii of Figures 6b, the resulting surface morphology, after DPV, shows more complete removal of Pb.

The change in the amount of Pb on the surface, expressed as a volume, was calculated from $1\text{ }\mu\text{m} \times 1\text{ }\mu\text{m}$ AFM images obtained prior to and after stripping. Cross-sectional height analysis of the Pb film was used for volume calculations at high concentrations (1 μM), whereas hemispherical NPs (vide supra) were assumed at the lower concentrations (100 and 10 nM). For 1 μM Pb (parts a(i) and b(i) of Figure 6), a $60 \pm 5\%$ reduction in volume, after stripping, was determined. The percentage removal increased to $91 \pm 5\%$ and $92 \pm 5\%$ for $[\text{Pb}^{2+}] = 100$ and 10 nM, respectively.

The significantly higher proportion of Pb left on the surface during the stripping step for 1 μM Pb²⁺ compared to the lower concentrations helps to explain the nonlinear calibration plot of charge (or peak current) versus $[\text{Pb}^{2+}]$ at high $[\text{Pb}^{2+}]$ (Figure 4b and Supporting Information, section 3). Incomplete anodic dissolution of electrodeposited Pb from pBDD electrode surfaces has previously been inferred in the literature, typically by considering

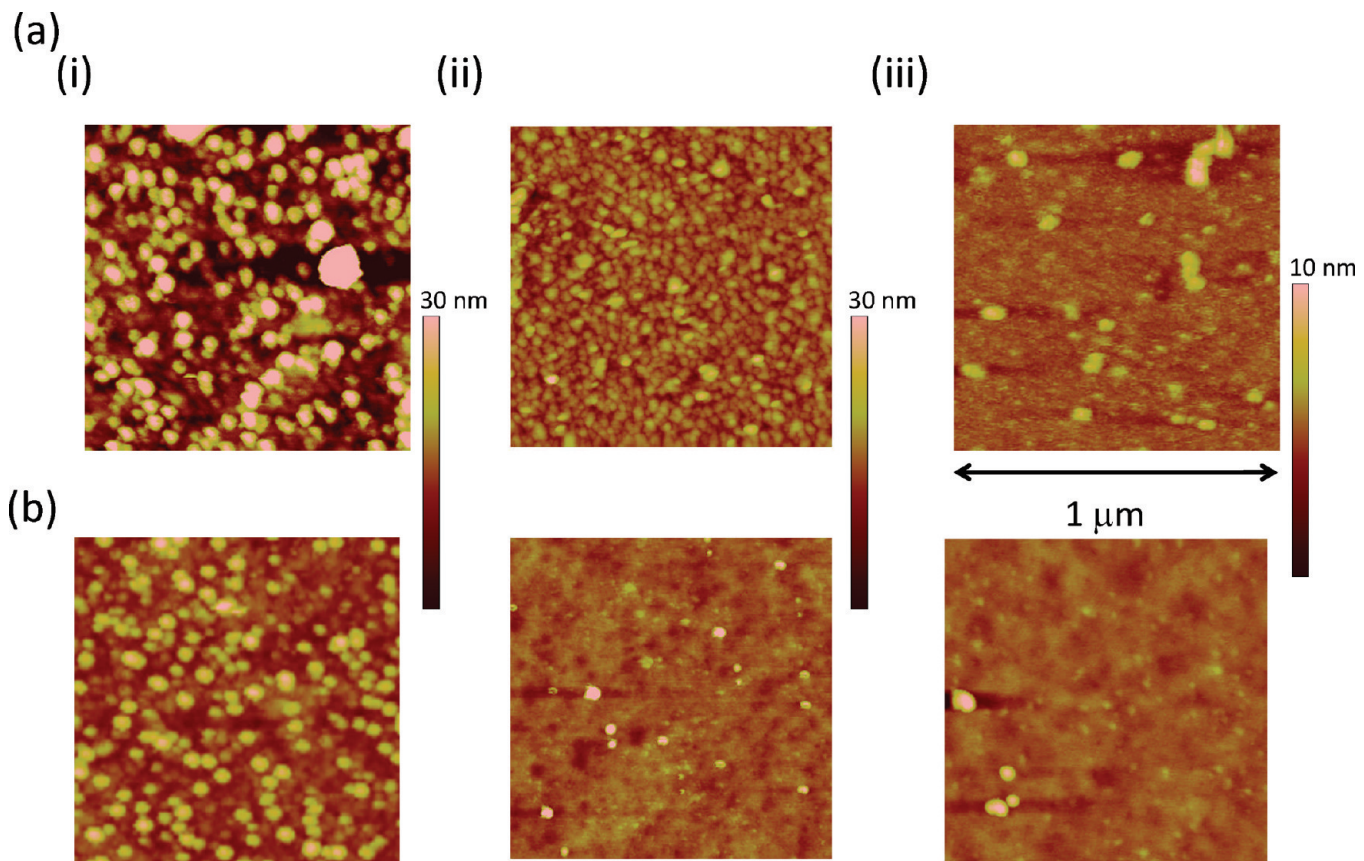


Figure 10. Typical $1\text{ }\mu\text{m} \times 1\text{ }\mu\text{m}$ in situ EC-AFM height images of the surface of a pBDD electrode after (a) Pb deposition for 400 s at -1.5 V (vs SCE) in stationary solution and (b) Pb stripping using DPV (pulse width, 50 mV; pulse amplitude, 50 mV; step size, 2 mV) in 0.1 M KNO_3 for (i) $10\text{ }\mu\text{M Pb}^{2+}$, (ii) $1\text{ }\mu\text{M Pb}^{2+}$, and (iii) $100\text{ }\text{nM Pb}^{2+}$. Images of deposition and stripping were recorded in the same location for the same concentration.

the charges associated with deposition and stripping,^{13,21,22,24} although this approach has also been disputed.¹⁵ In contrast, the AFM images in Figure 6 provide direct visual evidence that the amount of Pb deposited on the surface and the resultant surface morphology are significant factors in determining the extent to which Pb is subsequently removed and detected during DPV stripping.

Previous electrodeposition studies of Pt²⁰ and Ag⁴⁵ on pBDD have evidenced grain-dependent nucleation behavior, albeit at much lower driving forces.⁴⁰ Given the typical size of grains in pBDD,¹⁷ larger scan size ($5\text{ }\mu\text{m} \times 5\text{ }\mu\text{m}$) AFM images of the pBDD electrode surface were recorded after deposition using the impinging jet arrangement for $[\text{Pb}^{2+}] =$ (a) $1\text{ }\mu\text{M}$, (b) $100\text{ }\text{nM}$, and (c) $10\text{ }\text{nM}$ (Figure 7) to elucidate if this was the case for Pb at the concentrations and deposition conditions pertinent to stripping voltammetry.

For $1\text{ }\mu\text{M }[\text{Pb}^{2+}]$, Figure 7a shows a central structure, 25 nm in height, which is similar to the film-like topology observed in Figure 6a(i). Areas outside this region show the deposition of Pb NPs, with heights of $19 \pm 7\text{ nm}$ (SD) at a high density of $\sim 160\text{ }\mu\text{m}^{-2}$. At the lower $[\text{Pb}^{2+}]$ of $100\text{ }\text{nM}$ (Figure 7b), the NP surface coverages and heights are similar over the majority of the image. For example, the area outlined in white supports NPs of height $16 \pm 5\text{ nm}$ at $\sim 170\text{ }\text{NPs }\mu\text{m}^{-2}$, with surrounding areas supporting NPs $\sim 19 \pm 6\text{ nm}$ in height at $\sim 160\text{ }\text{NPs }\mu\text{m}^{-2}$. Only in a few isolated regions is the coverage so high that thin-film formation is favored. At $[\text{Pb}^{2+}] = 10\text{ }\text{nM}$ (Figure 7c), again there are no evident differences in deposit morphology for different pBDD grains.

Thus, in general, at $[\text{Pb}^{2+}] < 1\text{ }\mu\text{M}$, for the deposition times and potentials employed herein, there are no significant differences in metal deposition between different surface grains of pBDD. This contrasts with previous studies employing smaller deposition overpotentials and higher metal ion concentrations, where differences were seen,^{45,46} as the more conductive grains were able to support higher interfacial fluxes of metal ions.

The origin of the island-like Pb structure observed in Figure 7a is particularly interesting. To investigate this further, AFM studies were carried out under the same deposition conditions as for Figure 7a, but with shorter deposition times to capture the earlier stages of film growth. Figure 8a shows typical (i, ii) $3\text{ }\mu\text{m} \times 3\text{ }\mu\text{m}$ and (iii, iv) $5\text{ }\mu\text{m} \times 5\text{ }\mu\text{m}$ AFM images recorded after 300 s of $1\text{ }\mu\text{M Pb}^{2+}$ deposition at -1.5 V and Figure 8b a typical $5\text{ }\mu\text{m} \times 5\text{ }\mu\text{m}$ AFM image recorded after 400 s of Pb²⁺ deposition at -1.5 V .

As Figure 8a clearly shows, small circular-shaped islands have formed on the surface of an individual grain, which grow outward to merge with other islands, ultimately forming the structures shown in Figure 7a. In Figure 8b, two grains of different boron dopant densities are clearly present, as indicated by the clear step in height between grains (vide supra). Interestingly, the Pb island actually grows across the grain boundary from one grain to the next, with no significant change in the growth morphology, a process which is independent of the underlying boron doping level. Our many AFM and FE-SEM images recorded, from which it is possible to qualitatively infer differences in boron dopant levels (vide supra), indicate no preference for particular pBDD

grains during the initial stages of thin-film formation. Thus, we believe that, under the deposition conditions employed herein, differences in electrical characteristics associated with grains of different boron dopant levels do not play a significant role in Pb film formation.

The origin of the double stripping peak in previous DPV data on pBDD, seen here at higher $[Pb^{2+}]$, e.g., Figure 4a, has been either ignored¹³ or tentatively attributed to some aspect of the metal deposit on the electrode surface.¹⁵ Recent numerical simulations have shown that the morphology/structure of a metal deposit on an electrode surface will affect the stripping characteristics. In particular, it was shown numerically that the stripping response from hemispherically shaped deposits should occur at less positive potentials than that of a thin uniform film of the same mass, provided the particles are small, as is the case here.¹⁸

Thus, to investigate this aspect further, Figure 9 shows typical FE-SEM images recorded after Pb deposition at a range of concentrations, (a) 0.5 μM , (b) 10 μM , and (c) 30 μM , and the associated DPV response after Pb stripping. For all experiments, deposition was carried out for 400 s with the electrode held at -1.5 V . Note that the crystal-like features seen in the FE-SEM images are crystals of potassium nitrate that result when the sample was removed from solution, rinsed gently so as to not perturb the metallic deposits, and then left to dry.

It is strikingly clear that, when only NPs are formed in the deposition step, i.e., at the lower $[Pb^{2+}]$ (and/or deposition time), there is a single stripping peak in the DPV response. As $[Pb^{2+}]$ is increased and both NPs and thin-film-like structures are formed during electrodeposition, a second peak emerges in the DPV response, as also seen in Figure 4a and the Supporting Information, section 2. Indeed, at the highest concentration employed, where FE-SEM reveals the surface to be largely dominated by the film-like structures, the second stripping peak is significantly larger than the first peak. The images in Figure 9 thus suggest that the two peaks are intimately related to the different metal morphologies on the pBDD surface.

In Situ Electrochemical Atomic Force Microscopy (EC-AFM). To provide further information on the deposition and stripping behavior of Pb on pBDD, in situ EC-AFM was carried out so that the deposition morphology could be matched more closely with the resulting electrodissolution topography. However, as in situ EC-AFM is used in quiescent solution, the Pb^{2+} concentration was scaled up to compensate for the decreased mass transport rates during deposition. The focus of these experiments was on NP deposition and stripping.

Figure 10 shows typical $1 \times 1 \mu\text{m}$ in situ EC-AFM images for $[Pb^{2+}]$ = (i) 10 μM , (ii) 1 μM , and (iii) 100 nM after (a) deposition of Pb in quiescent solution (400 s at -1.5 V) and (b) DPV stripping of Pb from the surface. In each case, the deposition and stripping images were recorded in the same location. The deductions from the in situ experiments are as for the ex situ experiments. First, as $[Pb^{2+}]$ decreases, and the overall deposition flux decreases, the average height of the NPs decreases, here from $26 \pm 5.3\text{ nm}$ (10 μM) to $14 \pm 4.6\text{ nm}$ (1 μM) and finally to $8 \pm 2.3\text{ nm}$ (100 nM). Second, the volume of Pb removed from the pBDD surface after stripping increases as the concentration decreases, i.e., $63 \pm 3\%$ (10 μM), $93 \pm 5\%$ (1 μM), and $95 \pm 5\%$ (100 nM). This re-emphasizes that at high concentrations it is not always possible to remove all the deposited material in the stripping step, a point which needs to be carefully considered and addressed for heavy metal stripping voltammetry at solid electrodes. The in situ cleaning step described is also crucial for

obtaining a clean and reproducible surface prior to each measurement.

CONCLUSIONS

High-resolution microscopy techniques, including AFM and FE-SEM, have been utilized successfully to provide a greater understanding of the features observed by us and others in DPV-ASV of the popular Pb^{2+}/Pb system at pBDD, an example of a heterogeneous solid electrode. Significantly, the studies presented have allowed a comprehensive assessment of several long-standing questions in the literature, including the origin of the lower calibration gradients at low concentration, the observation of a second peak in the DPV response at higher concentrations, the nonlinear calibration gradient at high concentrations, and finally the effect, if any, of the varying electrical conductivity of the pBDD surface on the Pb deposition and stripping process.

DPV was implemented with hydrodynamic control using an impinging wall jet (during deposition) to deposit and detect Pb^{2+} (as Pb) quantitatively in the nanomolar (sub parts per billion) to micromolar concentration range. High driving potentials were employed to produce relatively homogeneous distributions of NPs on the surface, reflected in the narrow DPV stripping peaks observed.

In the low concentration regime, AFM revealed that the amount of Pb deposited on the surface, as estimated by AFM analysis, was lower than expected for simple convective-diffusive control of the deposition process. This was reflected in the reduced gradients of the calibration plots of the peak DPV current and/or DPV charge versus $[Pb^{2+}]$ in the lower concentration range. This highlights an important factor in stripping analysis at low concentration; i.e., complications are likely to arise from the nucleation and growth of NPs in this concentration regime, particularly finite induction kinetics which lead to complex variations in mass transport during the deposition step. This aspect of metal stripping analysis at solid electrodes requires further attention in general. As the concentration of Pb^{2+} was increased, AFM clearly showed that the size of the NPs deposited on the surface also increased. This correlated with a positive shift in the stripping peak potential which could thus be ascribed to an NP size-dependent redox potential for the Pb/Pb^{2+} couple.

FE-SEM and AFM revealed that the emergence of a second peak in the DPV, at higher $[Pb^{2+}]$, correlated with a change in the deposition morphology from small isolated NPs to heterogeneous structures comprising both thin films and NPs. The second peak was associated with stripping from the thin-film structures. This peak became larger the greater the extent of thin-film coverage and could even dominate the response.

AFM further revealed that increasing the amount of Pb on the pBDD surface made it more difficult to completely remove it all in one DPV sweep. Thus, a substantial amount of Pb could remain on the electrode surface, undetected by DPV. This was especially evident for extensive metal deposition, which produced the thin-film island morphologies and also explained the nonlinear calibration gradient at higher $[Pb^{2+}]$.

By comparing AFM and FE-SEM images, it was possible to qualitatively determine how the boron dopant levels varied across the surface of the pBDD due to differential boron uptake of different grains. In general, variations in the electrical conductivity of the pBDD surface played no role in the nucleation and growth morphologies observed.

Finally, for all of the studies described, an in situ electrochemical cleaning process was developed in which Pb could be

completely removed from the electrode surface. Initial studies focused on a cleaning period of 10 min, and it was shown that an electrode potential of +1.2 V after a stripping measurement was sufficient to create a clean surface for subsequent, repeat electroanalysis. AFM and XPS analysis confirmed that this procedure worked effectively at all concentrations to remove all electro-deposited Pb from the surface.

■ ASSOCIATED CONTENT

Supporting Information. Characterization of the hydrodynamics of the impinging flow wall-jet setup, determination of the radial position of average diffusion length at an impinging jet electrode, and DPV for Pb^{2+} concentrations in the range of 1–5 μM . This material is available free of charge via the Internet at <http://pubs.acs.org>.

■ AUTHOR INFORMATION

Corresponding Author

*E-mail: p.r.unwin@warwick.ac.uk (P.R.U.); j.macpherson@warwick.ac.uk (J.V.M.).

■ ACKNOWLEDGMENT

We acknowledge the support of EPSRC and BAE Systems (Mr. David Hankey) for the award of an EPSRC Industrial Case Studentship to L.A.H. Some of the equipment used in this work was obtained through the Science City Advanced Materials project with support from Advantage West Midlands and the European Regional Development Fund. We additionally thank Element Six Ltd. for the provision of high-quality pBDD samples, Dr. Lijaing Song (Warwick Chemistry) for help with the ICPMS analysis, and Dr. Ajay Shukla (Warwick Physics) for help with the XPS analysis.

■ REFERENCES

- (1) Wang, J. *Stripping Analysis: Principles, Instrumentation and Applications*; VCH: Deerfield Beach, FL, 1985.
- (2) (a) Daniele, S.; Mazzocchin, G. A. *Anal. Chim. Acta* **1993**, *273*, 3. (b) Wang, J.; Lu, J.; Chen, L. *Anal. Chim. Acta* **1992**, *259*, 123.
- (3) (a) Florence, T. M. *J. Electroanal. Chem. Interfacial Electrochem.* **1970**, *27*, 273. (b) Batley, G. E. *Anal. Chim. Acta* **1981**, *124*, 121. (c) Acebal, S. A.; Rebello, A. L. *Anal. Chim. Acta* **1983**, *148*, 71.
- (4) Wang, J. *Analytical Electrochemistry*, 2nd ed.; Wiley-VCH: New York, 2000.
- (5) Agra-Gutierrez, C.; Hardcastle, J. L.; Ball, J. C.; Compton, R. G. *Analyst* **1999**, *124*, 1053.
- (6) Brainina, K. Z.; Kubysheva, I. V.; Miroshnikova, E. G.; Parshakov, S. I.; Maksimov, Y. G.; Volkonsky, A. E. *Field Anal. Chem. Technol.* **2001**, *5*, 260.
- (7) Pleskov, Y. V. *Russ. J. Electrochem.* **2002**, *38*, 1275.
- (8) Xu, J. S.; Granger, M. C.; Chen, Q. Y.; Strojek, J. W.; Lister, T. E.; Swain, G. M. *Anal. Chem.* **1997**, *69*, A591.
- (9) Compton, R. G.; Foord, J. S.; Marken, F. *Electroanalysis* **2003**, *15*, 1349.
- (10) Ramesham, R.; Rose, M. F. *Diamond Relat. Mater.* **1997**, *6*, 17.
- (11) Dragoe, D.; Spataru, N.; Kawasaki, R.; Manivannan, A.; Spataru, T.; Tryk, D. A.; Fujishima, A. *Electrochim. Acta* **2006**, *51*, 2437.
- (12) McGaw, E. A.; Swain, G. M. *Anal. Chim. Acta* **2006**, *575*, 180.
- (13) Manivannan, A.; Tryk, D. A.; Fujishima, A. *Electrochim. Solid-State Lett.* **1999**, *2*, 455.
- (14) Babyak, C.; Smart, R. B. *Electroanalysis* **2004**, *16*, 175.
- (15) Sonthalia, P.; McGaw, E.; Show, Y.; Swain, G. M. *Anal. Chim. Acta* **2004**, *522*, 35.
- (16) Tsai, Y.-C.; Coles, B. A.; Holt, K.; Foord, J. S.; Marken, F.; Compton, R. G. *Electroanalysis* **2001**, *13*, 831.
- (17) Wilson, N. R.; Clewes, S. L.; Newton, M. E.; Unwin, P. R.; Macpherson, J. V. *J. Phys. Chem. B* **2006**, *110*, 5639.
- (18) Ward Jones, S. E.; Toghill, K. E.; Zheng, S. H.; Morin, S.; Compton, R. G. *J. Phys. Chem. C* **2009**, *113*, 2846.
- (19) McAuley, C.; Banks, C. E.; Simm, A. O.; Jones, T. G. J.; Compton, R. G. *Analyst* **2006**, *131*, 106.
- (20) Hutton, L.; Newton, M. E.; Unwin, P. R.; Macpherson, J. V. *Anal. Chem.* **2009**, *81*, 1023.
- (21) Hyde, M. H.; Jacobs, R.; Compton, R. G. *J. Phys. Chem. B* **2002**, *106*, 11075.
- (22) Goeting, C. H.; Foord, F. J.; Eklund, J. C.; Marken, F. M.; Compton, R. G.; Chalker, P. R.; Johnson, C. *J. Electroanal. Chem.* **1998**, *442*, 207.
- (23) Zhu, P.; Zhu, J.; Yang, S.; Zhang, X.; Zhang, G. *Fresenius' J. Anal. Chem.* **1995**, *353*, 171.
- (24) Awada, M.; Strojek, J. W.; Swain, G. M. *J. Electrochem. Soc.* **1995**, *142*, L42.
- (25) Vinokur, N.; Miller, B.; Avyigal, Y.; Kalish, R. *J. Electrochem. Soc.* **1999**, *146*, 125.
- (26) Nakabayashi, S.; Tryk, D. A.; Fujishima, A.; Ohta, N. *Chem. Phys. Lett.* **1999**, *300*, 409.
- (27) Omanovic, D.; Peherac, Z.; Magier, T.; Lovric, M.; Branica, M. *Electroanalysis* **2005**, *6*, 1029.
- (28) Saterlay, A. J.; Agra-Gutierrez, C.; Taylor, M. P.; Marken, F.; Compton, R. G. *Electroanalysis* **1999**, *11*, 1083.
- (29) Saterlay, A. J.; Foord, J. S.; Compton, R. G. *Analyst* **1999**, *124*, 1791.
- (30) Saterlay, A. J.; Marken, F.; Foord, J. S.; Compton, R. G. *Talanta* **2000**, *53*, 403.
- (31) Banks, C. E.; Hyde, M. E.; Tomcik, P.; Jacobs, R.; Compton, R. G. *Talanta* **2004**, *62*, 279.
- (32) (a) Macpherson, J. V.; Marcar, S.; Unwin, P. R. *Anal. Chem.* **1994**, *66*, 2175. (b) Macpherson, J. V.; Beeston, M. A.; Unwin, P. R. *J. Chem. Soc., Faraday Trans.* **1995**, *91*, 899. (c) Martin, R. D.; Unwin, P. R. *J. Electroanal. Chem.* **1995**, *397*, 323.
- (33) Melville, J. L.; Coles, B. A.; Compton, R. G.; Simjee, N.; Macpherson, J. V.; Unwin, P. R. *J. Phys. Chem. B* **2003**, *107*, 379.
- (34) Bitziou, E.; Rudd, N. C.; Edwards, M. A.; Unwin, P. R. *Anal. Chem.* **2006**, *78*, 1435.
- (35) Miller, J. B.; Brandes, G. R. *J. Appl. Phys.* **1997**, *82*, 4538.
- (36) Janssen, G.; van Enckevort, W. J. P.; Vollenberg, W.; Giling, L. J. *Diamond Relat. Mater.* **1992**, *1*, 789.
- (37) Hird, J. R.; Field, J. E. *Proc. R. Soc. London, A* **2004**, *460*, 3547.
- (38) Albery, W. J.; Brett, C. M. A. *J. Electroanal. Chem.* **1983**, *148*, 201.
- (39) Liu, F. B.; Wang, J. D.; Liu, B.; Li, X. M.; Chen, D. R. *Diamond Relat. Mater.* **2007**, *16*, 454.
- (40) Song, Y.; Swain, G. M. *Anal. Chem.* **2007**, *79*, 2412.
- (41) Fransaer, J. L.; Penner, R. M. *J. Phys. Chem. B* **1999**, *103*, 7643.
- (42) (a) Henglein, A. *J. Phys. Chem.* **1993**, *97*, 5457. (b) Ward Jones, S. E.; Toghill, K. E.; Zheng, S. H.; Morin, S.; Compton, R. G. *J. Phys. Chem. C* **2009**, *113*, 2846.
- (43) Oldham, H. B.; Myland, J. C. *Fundamentals of Electrochemical Science*; Academic Press: New York, 1994.
- (44) *Handbook of Chemistry and Physics*, 89th ed.; Lide, D. R., Ed.; CRC Press: Boca Raton, FL, 2008.
- (45) Colley, A. L.; Williams, C. G.; Johansson, U. D.; Newton, M. E.; Unwin, P. R.; Wilson, N. R.; Macpherson, J. V. *Anal. Chem.* **2006**, *78*, 2539.
- (46) Simm, A. O.; Ji, X.; Banks, C. E.; Hyde, M. E.; Compton, R. G. *ChemPhysChem.* **2006**, *7*, 704.